Int. J. Electrochem. Sci., 13 **(2018)** 2800 – 2816, doi: 10.20964/2018.03.50

International Journal of
ELECTROCHEMICAL
SCIENCE
www.electrochemsci.org

Preparation and Characterization of Activated Carbons from Oxygen-rich Lignite for Electric Double-layer Capacitor

Xiao-Yan Zhao, Yan Wu, Jing-Pei Cao[*], *Qi-Qi Zhuang, Xiao Wan, Shan He, Xian-Yong Wei*

Key Laboratory of Coal Processing and Efficient Utilization (Ministry of Education), China University of Mining & Technology, Xuzhou 221116, Jiangsu, China
[*]E-mail: caojingpei@cumt.edu.cn, beyondcao@hotmail.com

Received: 21 November 2017 / *Accepted:* 8 January 2018 / *Published:* 5 February 2018

Activated carbons (ACs) were derived from oxygen-rich lignite via chemical activation for electric double-layer capacitor (EDLC). The preparation parameters affect the pore structure and specific surface area of ACs were discussed in this work. The pores of the ACs are mainly micropores and the functional groups of ACs are not changed compared with SL. When the carbonized temperature is 700 ^{o}C, activated temperature is 800 ^{o}C and KOH/char ratio is 4, the AC is rich in C-O, C=O and -COOH species, exhibits excellent electrochemical performance with the maximum specific capacitance of 213 F g^{-1} in 6 M KOH at the current density of 40 mA g^{-1}. Furthermore, the electrode exhibits excellent cycle stability. Therefore, the AC electrodes derived from lignite are promising candidates for EDLC.

Keywords: Activated carbons, Oxygen-rich lignite, Electric double-layer capacitor

1. INTRODUCTION

Electric double-layer capacitor (EDLC) also called supercapacitor has attracted much attention owing to its high power, energy density and high cycle capacity [1-3]. And as an energy storage device, the application of EDLC is widely such as communication devices, electronic devices and hybrid electrical [4-6]. The core component of the EDLC is the electrode materials. Much effort has been focused on developing flexible EDLC materials [7] which have high electrochemical capacitance and mechanical strength, such as activated carbons (ACs) [8], graphene [9], carbon nanofibers [10] and carbon aerogels [11]. Among these materials, the ACs expected to be the ideal materials used for EDLC due to its good conductivity, high specific surface area (SSA), and moderate cost. The ACs can be prepared from a variety of precursors via heat treatment with activation agents.

Coal is most commonly used to prepare the ACs due to its abundance, cheapness and high carbon content. Zhao et al. [12] used HyperCoal as raw materials through conventional 2-step

carbonization/KOH-activation method to prepared ACs and obtained the specific capacitance as high as 46.0 F g^{-1} in 0.5 M $TEABF_4$/PC. Gryglewicz et al. [13] used the sulfonated subbituminous coal as the precursor to preparation a series of ACs for EDLC and the highest capacitance exceed 160 F g^{-1} in H_2SO_4 electrolytic solution. Compared with bituminous coal and HyperCoal, lignite has high oxygen content. The surface wettability of the ACs could be enhanced by the adequate oxygen-containing species (OCSs) and then the exposed surface could be sufficiently utilized for charge storage. The heteroatoms or oxygen-rich functional group are commonly introduced or graft into the ACs aims to improve the wettability and contribute pseudocapacitance [14-16]. The materials with abundant of functional group as the precursor to prepare ACs have attracted much attention. Lignite has high moisture content, high amount of volatiles and high amount of oxygen-containing species (OCSs). In particular, the O/C ratio of lignite is the highest in all the coal ranks. And the OCSs in the lignite can be categorized into carboxyl, hydroxyl, carbonyl and ether functionalities. And the OCS in lignite is mainly present in carboxyl, hydroxyl, carbonyl and ether functionalities. Nearly 50% of the oxygen in lignite is present in the form of carboxyl and hydroxyl [17, 18]. Lignite with a wealth of OCSs is considered to be a promising alternative candidate to prepared ACs as electrode materials for EDLC.

There are two methods to prepare ACs: physical activation and chemical activation. Whereas, chemical activation is considered an effective methods to create pores [19]. Among various activating agents, KOH was widely used to process ACs to deliver porosity and thus to enhance EDLC performances [20, 21]. In this work, ACs were prepared from oxygen-rich lignite by KOH activation. The influence of the carbonized temperature, activated temperature and KOH/char ratio on the pore structure and SSA of ACs were investigated. X-ray diffraction (XRD), Scanning electron microscope (SEM) and N_2 adsorption-desorption were used to characterized the morphology and structure of the obtained ACs. The OCSs of material was measured by Fourier transform infrared spectroscopy (FTIR) and X-ray photoelectron spectroscopy (XPS). The electrochemical performances of the EDLC were characterized by galvanostatic charge-discharge (GCD), cyclic voltammetry (CV), electrochemical impedance spectroscopy (EIS) and cycling durability.

2. EXPERIMENTAL

2.1 Materials

The oxygen-rich Shengli lignite (SL) was collected from Inner Mongolia, China. It was pulverized to pass through a 200 mesh sieve following by drying at 107 ^oC for 24 h. The SL contains 18.72% ash, 43.64% volatile matter and 37.64% fixed carbon (wt%, dried basis). The elemental content (wt%, dry and ash-free basis) of C, H, N, S and O are 67.47%, 4.96%, 1.27%, 0.52% and 25.78%, respectively [22]. The SL was characterized by a Thermo ESCALAB 250Xi apparatus. The relative content of functional group in XPS spectra is listed in Table 1 and the high-resolution XPS spectra of O1s of SL is shown in Fig. 1. The O 1s in Fig.1 can be resolved into three individual component peaks, which are C=O bonds (O1, 531.5 eV), C-O bonds (O2, 532.4 eV) and COO- bonds (O3, 533.3 eV).

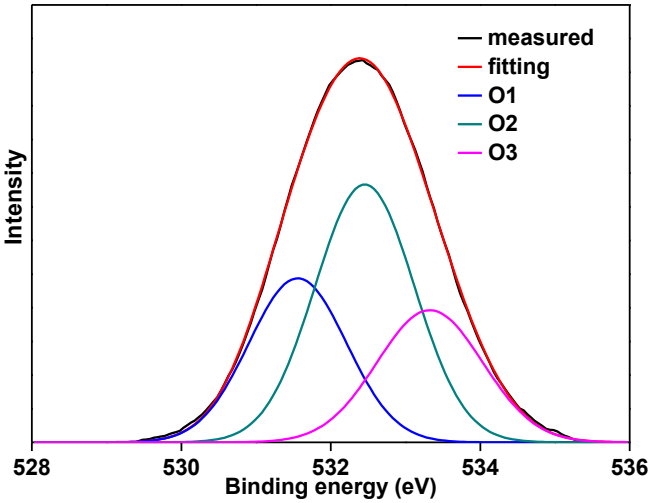

Figure 1. High-resolution XPS spectra of O1s of SL.

Table 1. Relative contents of functional groups in XPS spectra of SL.

Sample	C/O[a]	C1s					O1s		
		C1 (%)	C2 (%)	C3 (%)	C4 (%)	C5 (%)	O1 (%)	O2 (%)	O3 (%)
SL	1.62	39.18	27.28	18.46	8.62	6.46	28.79	46.07	25.14

[a] Atomic ratio.

Table 2. Preparation parameters of ACs samples.

Sample	CT (^{o}C)	AT (^{o}C)	Ratio
AC-H-500	500	800	2
AC-H-600	600	800	2
AC-H-700	700	800	2
AC-H-800	800	800	2
AC-H-900	900	800	2
AC-500	700	500	2
AC-600	700	600	2
AC-700	700	700	2
AC-800	700	800	2
AC-900	700	900	2
AC-K-2	700	800	2
AC-K-3	700	800	3
AC-K-4	700	800	4
AC-K-5	700	800	5

CT: Carbonized temperature; AT: Activated temperature; AC-H-700=AC-800=AC-K-2.

2.2 Preparation of ACs

The ACs were prepared by traditional two-step method. First, the SL was carbonized in different temperatures (500-900 ^{o}C) under Ar flow and subsequently cooled to room temperature to obtain char. Then the char was mixed with KOH and activated in a horizontal tube furnace at the final temperature (500-900 ^{o}C) for 2 h in an Ar atmosphere. The activation samples were washed with 2 M

HCl solution and deionized water until the filtrate became neutral. Then the samples were dried at 200 ^{o}C in a vacuum oven for 2 h. The ACs prepared from different carbonized temperatures were named AC-H-X, where the X refers to the carbonized temperature. The ACs derived from different activated temperatures and different KOH/char ratios were denoted as AC-Y and AC-K-Z, where Y refers to the activated temperature and Z refers to the ratio of KOH/char, respectively. All the samples and their preparation parameters in this study are shown in Table 2. The yields of char (carbonized process) and ACs (activated process) were calculated according to Eqs. (1) and (2), respectively.

$$Y_1 = \frac{m_1}{m_2} \times 100\% \quad (1)$$

$$Y_2 = \frac{m_3}{m_1} \times 100\% \quad (2)$$

Where m_1 is the weight of char, m_2 and m_3 are the weight of SL and AC, respectively.

2.3 Characterization

XRD scattering was obtained on a Bruker D8 ADVANCE with Cu Kα radiation. A Merlin Zeiss SEM was employed to investigate the feature of samples. XPS spectra was characterized using a Thermo ESCALAB 250Xi apparatus. The surface functional groups were measured with a Nicolet Magna 560 FTIR. N_2 adsorption-desorption isotherms were observed with a Quantachrome Autosorb-IQ automated gas sorption analyzer which using N_2 as the adsorbate at -196 ^{o}C. The SSA was calculated by Brunauer-Emmett-Teller (BET) equation and the pore size distribution was obtained using Density Functional Theory (DFT) method.

2.4 Electrochemical measurement

The EDLC electrodes were made by mixture of AC (87 wt%), acetylene black (10 wt%) and polytetrafluoroethylene (PTFE, 3 wt%). Then the homogeneous mixture was pressed on nickel foam current collector. Before electrochemical tests, electrodes and the polypropylene membrane were immersed with 6 M KOH solution under vacuum for 24 h. The capacitor was assembled in 6 M KOH solution with two AC electrodes (about 30 mg of activated materials in each electrode).

The electrochemical measurement of electrodes was carried out by IVIUM electrochemical working station at room temperature. The CV measurement was performed at a voltage between 0 and 1 V with different sweep rates. EIS analysis was conducted using frequency ranging from 10^{-2} to 10^{5} Hz with alternate current amplitude of 10 mV. GCD measurement was run on different current densities in a voltage rang of 0 to 0.8 V at different current densities by NEWARE cell test instrument. The specific capacitance was deduced from the Eq. (3).

$$C_s = 2\frac{I\Delta t}{m\Delta V} \quad (3)$$

In which C_s is the specific capacitance (F g^{-1}), I is the discharge current (A), Δt is the discharge time (s), and m is the mass of the activated material in single electrode (g), ΔV is the voltage difference (V).

3. RESULTS AND DISCUSSION

3.1 Physicochemical characteristics of ACs

3.1.1 XRD and SEM analyses of ACs

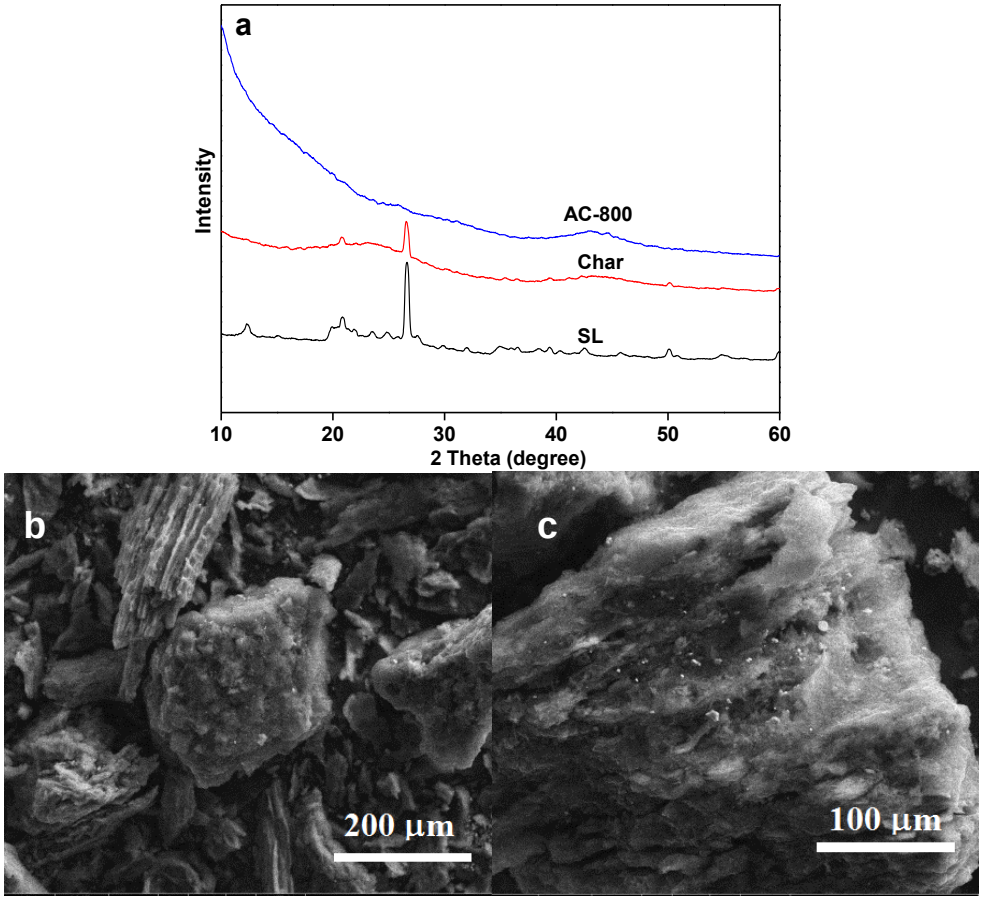

Figure 2. XRD patterns of samples (a) and SEM images of AC-800 (b and c).

The XRD patterns of SL, char (carbonized at 700 ^{o}C) and AC-800 are shown in Fig. 2a. SL shows a sharp peak at approximately 26^{o}, corresponding to the (002) layer of graphite [23], indicating that there is mainly microcrystalline graphitic structure in SL. The diffraction peak at 26^{o} becomes weak after carbonization at 700 ^{o}C and even disappears after activated with KOH (AC-800). In addition, a new broaden weak diffraction peak of the char and AC-800 can be observed at $2\theta = 43^{o}$, corresponding to the (100) diffraction of graphitic carbon with the amorphous character [24]. The reason may be that the structure of SL is destroyed to form amorphous carbon at high temperature (700 ^{o}C) and the crystalline structures have been destroyed due to the KOH etching in the chemical activation process. Compared to char and SL, the XRD curve of AC-800 increased rapidly at the low-angle scatter, suggesting the presence of a high density of pores [21].

The surface morphology of the AC-800 is characterized by SEM, which is shown in Fig. 2c. It can be seen that highly porous and honeycomb structure with some overgrown clusters existed on the

particle surface. The highly porous structure is beneficial to the electrolyte ions transmission during the charge-discharge progress [25].

3.1.2 FTIR and XPS analyses of ACs

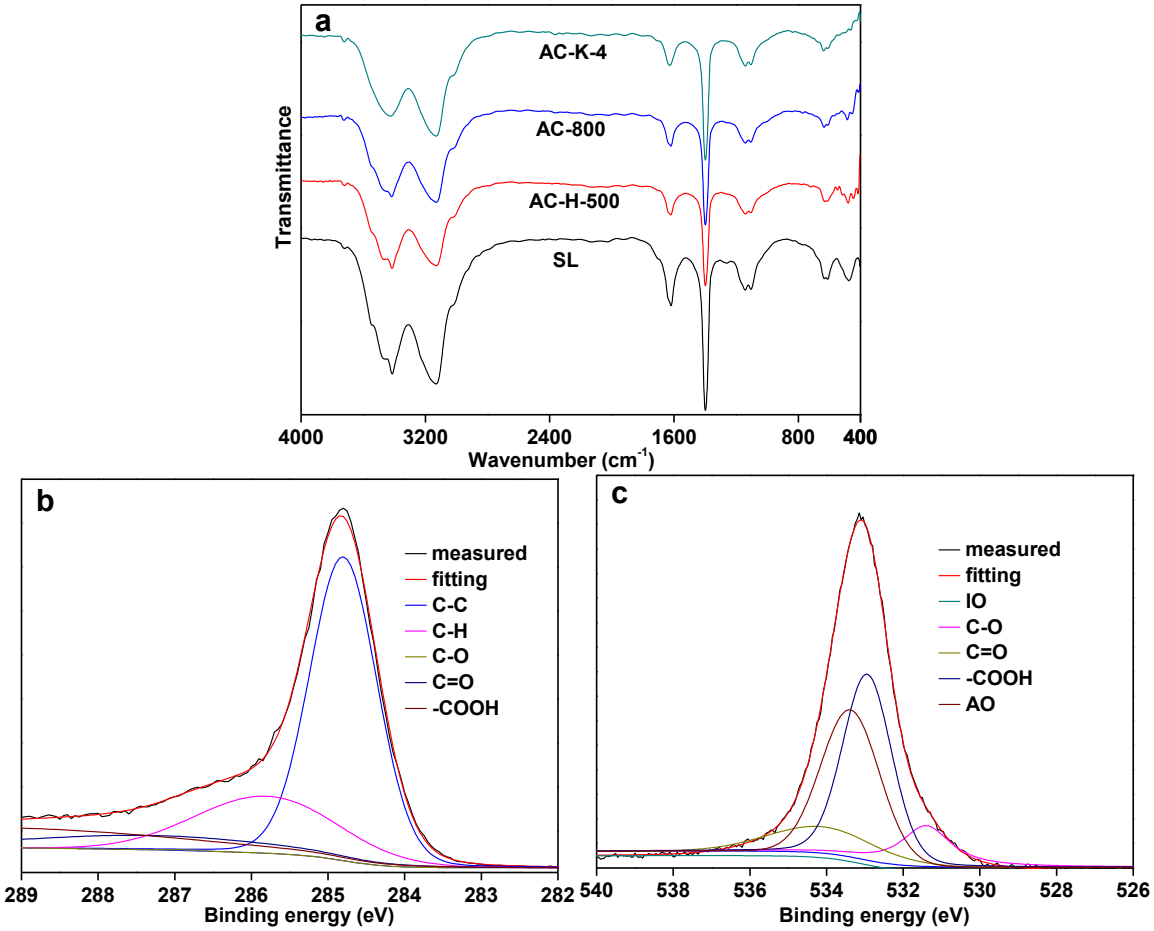

Figure 3. FTIR spectra of samples (a) and XPS spectra of AC-K-4: C 1s (b) and O 1s (c).

FTIR spectroscopy is applied to characterize the functional groups of the samples. In the spectra shown in Fig. 3a, the strong absorbance around 3403 cm^{-1} is attributed to bound -OH and the band at around 1613 cm^{-1} is assigned to the stretching of aromatic rings [26]. The peaks at 1400 cm^{-1} and 1106 cm^{-1} are attributed to C-H asymmetrical bending and C-O stretching [27, 28], respectively. Compared to SL, the functional groups in ACs are not changed demonstrating that the KOH has little effect on the functional groups at activated process. XPS is a surface-sensitive technique to study the functional groups of material. Figs. 3b and 3c show the high-resolution C 1s and O 1s of AC-K-4 and the elemental composition is shown in Table 3. The form of the oxygen in the AC surface is mainly C-O (531.4 eV), C=O (532.1 eV) and -COOH (532.9 eV). The present of oxygen in AC might enhanced the wettability and afford the pseudo-capacitance through faradaic charge-transfer reactions [29, 30].

The high-resolution C 1s peak (Fig. 3b) is related to C-C bonds (C1, 284.8 eV), C-H bonds (C2, 285.8 eV), C-O (C3, 286.9 eV), C=O bonds (C4, 287.3 eV) and COO- bonds (C5, 289.3 eV),

respectively. The O 1s (Fig. 3c) is resolved into five component peaks, i.e., IO (IO: inorganic oxygen) bonds (O1, 530.3 eV), C=O bonds (O2, 531.4 eV), C-O bonds (O3, 532.1 eV), -COOH (O4, 532.9 eV) and AO (AO: adsorbed oxygen) bonds (O5, 533.38 eV). The relative contents of C 1s and O 1s are listed in Table 3.

Table 3. Relative contents of functional groups in XPS spectra.

Sample	C 1s					O 1s				
	C1 (%)	C2 (%)	C3 (%)	C4 (%)	C5 (%)	O1 (%)	O2 (%)	O3 (%)	O4 (%)	O5 (%)
AC-K-4	52.64	20.39	0.06	9.05	17.85	41.72	7.11	6.75	23.44	20.98

Table 4. Pore structure parameters of ACs.

Sample	S_{BET} (m^2 g^{-1})	V_{total} (cm^3 g^{-1})	D_{ave} (nm)	Y_1 (%)	Y_2 (%)	Y_{total} (%)	C_g (F g^{-1})
AC-H-500	1244	0.58	1.87	78.3	46.9	36.7	165
AC-H-600	1606	0.81	2.40	72.6	47.1	34.2	190
AC-H-700	1732	0.82	1.86	68.8	50.4	34.6	195
AC-H-800	1156	0.65	1.12	65.9	55.3	36.4	168
AC-H-900	862	0.57	2.65	63.1	61.9	39.0	163
AC-500	625	0.31	2.01	68.8	89.0	61.2	109
AC-600	924	0.39	1.69	68.8	72.4	49.8	132
AC-700	1368	0.71	2.07	68.8	65.7	45.2	174
AC-800	1732	0.82	1.86	68.8	50.4	34.6	195
AC-900	1326	0.76	2.91	68.8	45.7	31.4	187
AC-K-2	1732	0.82	1.86	68.8	50.4	34.6	195
AC-K-3	2086	0.96	1.86	68.8	46.2	31.7	204
AC-K-4	2550	1.24	1.94	68.8	41.2	28.3	213
AC-K-5	1645	0.76	1.85	68.8	39.5	27.1	177

3.1.3 Porous structure of ACs

The preparation process conditions of ACs have a great influence on the pore structure. In this study, the effects of preparation parameters including carbonized temperature, activated temperature and the weight ratio of KOH/char on the pore structure are investigated. As shown in Table 4, the SSA and total pore volume increased with the carbonized temperature from 500 to 700 ^oC and decreased when the temperature over 700 ^oC. With the carbonized temperature increasing, the volatiles in SL are gradually released and leaving a lot of pore. KOH enters the pore and reacts with the carbon atoms in SL. However, the carbon atoms which can react with KOH are reduced when the carbonized temperature is over 700 ^oC, leading to the decrease of the SSA and total pore volume.

As shown in Fig. 4a, all the samples exhibit type I isotherm curves according to the IUPAC classification, showing that mainly microporous existed in the ACs [31], which also can be obtained from the pore size distribution (Fig. 5a). The pore size of the ACs with different carbonized temperatures is mainly in 0.4-2.0 nm and secondary in 2.0-5.0 nm, which is benefit for the electrolyte transmission and to form an electric double layer on the electrode surface [15].

The isotherms of ACs with different activated temperatures are shown in Fig. 4b. The N_2 adsorption increase quickly under low relative pressures. Then a horizontal adsorption platform presents at high P/P_0, demonstrating that the pore structure of the ACs is mainly microporous [24]. The adsorption capacity of ACs increased with the activated temperature from 500 to 800 ^oC and further decreased when activated temperature is up to 900 ^oC, which is consistent to the SSA result exhibited in Table 4. The activation process between KOH and carbon atoms has been reported [32]

$$6KOH+2C \rightarrow 2K_2CO_3 +2K+3H_2 \quad (4)$$

Then the decomposition of K_2CO_3 or reaction with carbon atoms to form $K/K_2O/CO_2$, simultaneously. The reaction between KOH and C requires high energy.

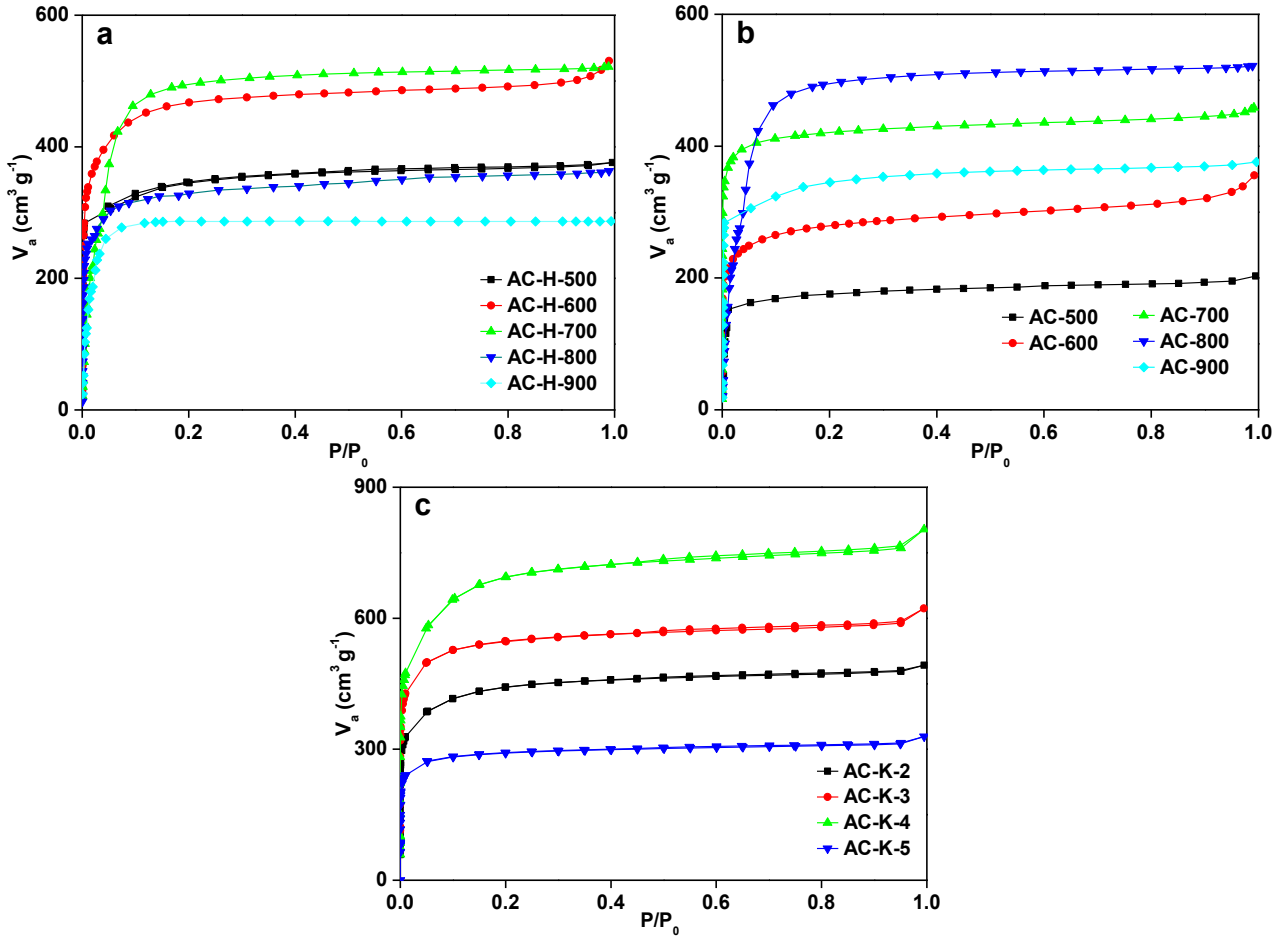

Figure 4. The N_2 isotherms of ACs with different conditions: different carbonized temperatures (a), different activated temperatures (b) and different KOH/char ratios (c).

Enough energy could be provided in the high activated temperature which leading to the activated reaction more completely. What is more, the reaction become intensified with the activation temperature increases, which leading to widen the pore size, enlarge the SSA and pore volume. Therefore, it will produce an increasing SSA with increasing activated temperature. But, the pore structure may collapsed at excessive activated temperature and leading to decrease of SSA [25]. With activated temperature increasing, the peak value of micropores in the pore size distribution (Fig. 5b)

shows slightly increased from 0.60 nm to 0.99 nm and the pore size in 2.0-5.0 nm. Generally, the pore development can be divided into three stages [33]: (1) opening of previously inaccessible pores, (2) creating of new pores, (3) widening of the existing pores. Pore widening may play a domination role with the increasing activated temperature.

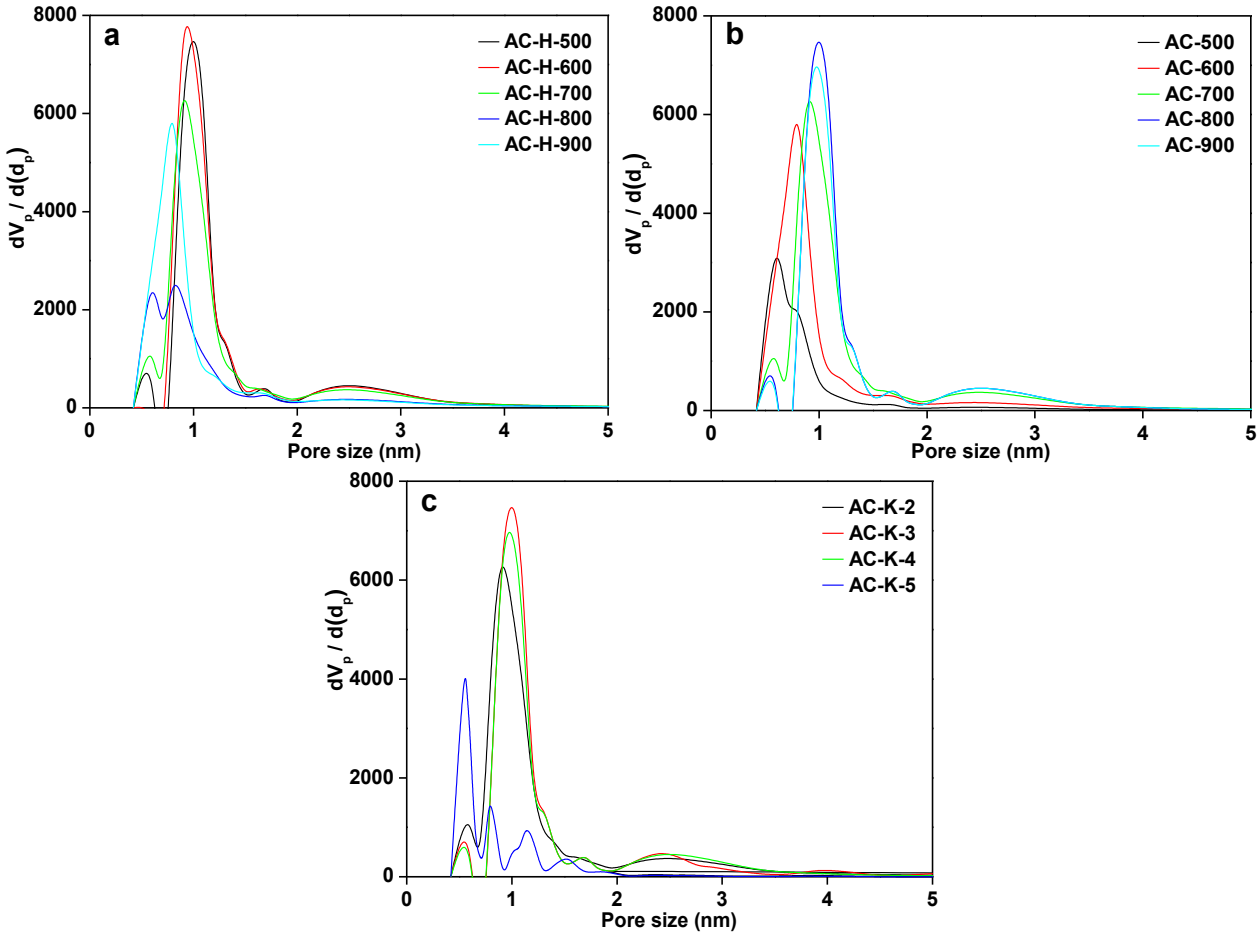

Figure 5. Pore size distribution of ACs with different conditions: different carbonized temperatures (a), different activated temperatures (b) and different activation ratios (c).

Fig. 4c shows the N_2 adsorption-desorption isotherm curves of ACs with different activation ratios. The SSA slightly increases with increasing KOH/char ratio from 2 to 4 and then decreases above 4 (Table 4). The maximum SSA reached 2550 m^2 g^{-1}. The porosity containing micropores and either meso- or macro-pores is believed to be ideal [34]. The activation by KOH may make micropores etched into mesopores or macropores, however, the excessive KOH could lead to pore collapse and result in a reduction of SSA [25]. At a relatively low KOH/char ratio is mainly micropores formation. The micropores come from the formation of new pores and the opening of previously inaccessible pores. Whereas, at the high ratio of KOH/char, the pore widening take the domination in the reaction. The pore size of the ACs with different ratios is mainly focus on 0.42-3.35 nm (Fig. 5c). When the ratio is raised up to 4, the reagent is enough for pore widening leading to a large pore size (D_{ave} = 1.94 nm). The SSA and the total volume decreased when further raising the ratio, which is probably attributed to the excessive KOH leading the pore collapse.

3.2 Electrochemical performances of ACs

3.2.1 GCD measurement

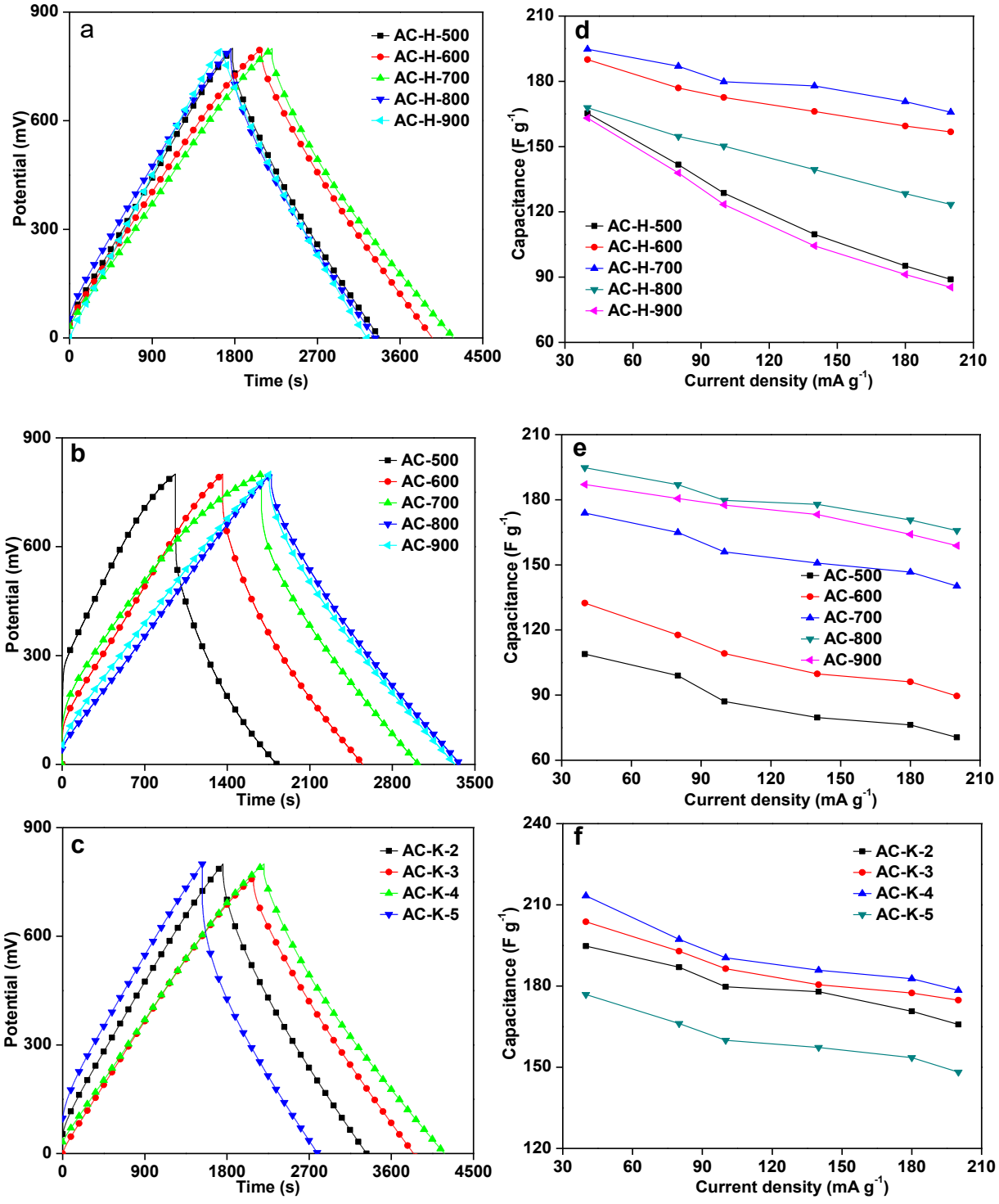

Figure 6. GCD curves of AC electrodes at the current density of 40 mA g^{-1} (a, b and c) and the specific capacitance of ACs at different current densities (d, e and f).

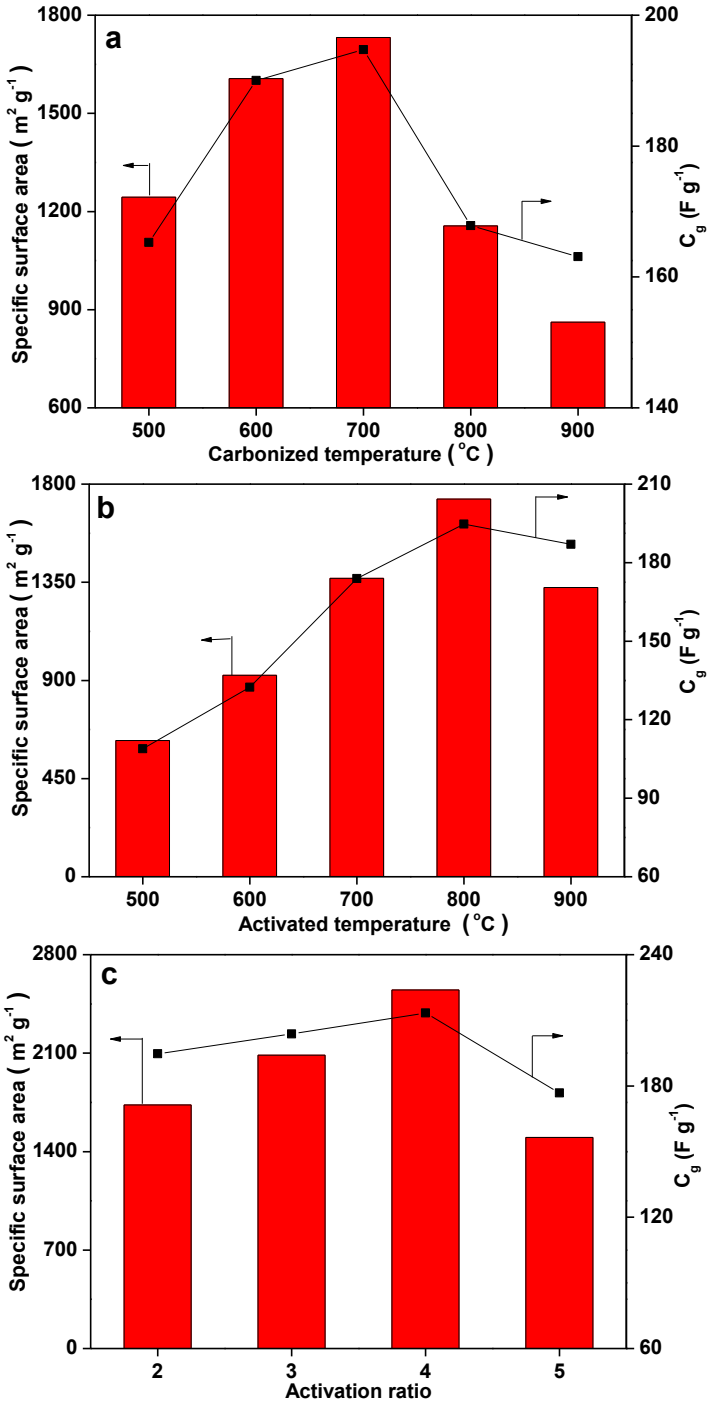

Figure 7. The specific capacitance and SSA of ACs: different carbonized temperatures (a), activated temperatures (b) and activation ratios (c)

GCD curves at the current density of 40 mA g^{-1} are presented in Fig. 6. All the GCD curves of AC electrodes under different preparation conditions exhibit regular triangular-shapes with IR voltage drops, which indicate the good EDLC behaviors [35]. As shown in Fig. 6a, the GCD curves of AC-H-700 is much longer than others, demonstrating that the AC-H-700 has higher specific capacitance than others at the same current density. The reason is that the AC-H-700 has the largest SSA. The high specific capacitance is usually obtained at high SSA [36].

As shown in Fig. 7, the specific capacitance increased with the increase of SSA. The SSA of AC-H-500 is higher than AC-H-900. However, the specific capacitances of the ACs are almost the same, which should be due to the difference in pore size. The average pore size (Table 4) of AC-H-900 is larger than that of AC-H-500 and this is benefit to the transport of electrolyte ion and result in the high specific capacitance of AC-H-900 at low SSA. Fig. 6b shows the GCD curves of ACs at different activated temperatures. The charge curves are slight winding and the time of charge is longer than the discharge, especially when the activated temperature below 700 ^{o}C. The SL is rich in OCSs and the activation is incomplete at low temperature. A part of OCSs occur irreversible oxidation reaction at the charge process which leading the charging time longer than the discharge. Some OCSs improve the wettability of ACs and increase the specific capacitance. The SSA of AC-500 is only 625 m^2 g^{-1} while the specific capacitance is as high as 109 F g^{-1}. Fig. 6c shows the GCD curves at the current density of 40 mA g^{-1} of ACs with different KOH/char ratios. The SSA and specific capacitance increased with KOH/char ratio range from 2 to 4 and decreased when the ratio is over 4 (Fig. 7c). The maximum specific capacitance of 213 F g^{-1} is obtained at the KOH/char ratio of 4. The pore of ACs with different KOH/char ratios is mainly in 1.0 nm, which is benefit to the electrolyte ions transport in the ACs [37, 38]. However, the excess KOH could lead the over ablation and cause the pore collapse.

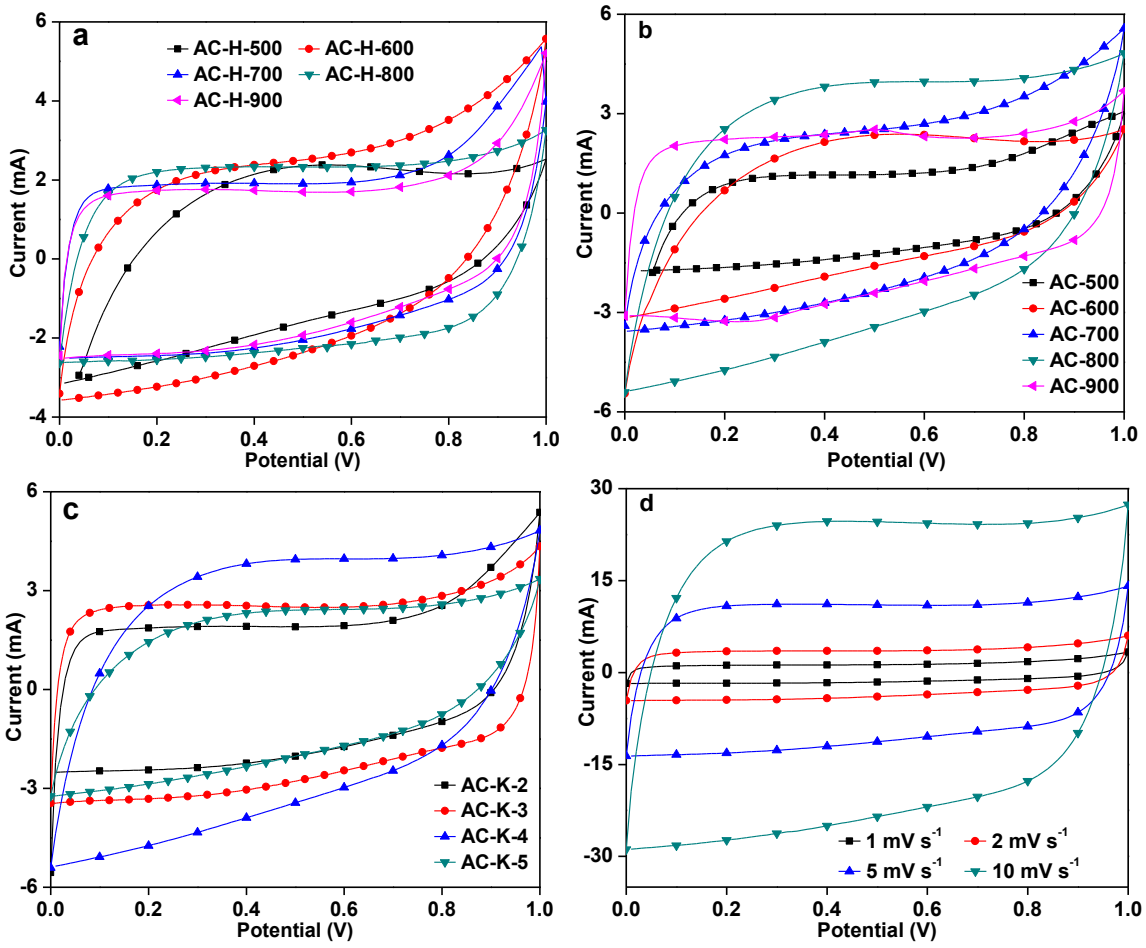

Figure 8. CV curves of AC electrodes at the scan rate of 1 mV s^{-1}: different carbonized temperatures (a), activated temperatures (b) and activation ratios (c), CV curves of AC-K-4 electrode at different scan rates (d).

The specific capacitance at different current densities is displayed in Figs. 6d-6f. The specific capacitances slightly decrease with the current density increased from 40 to 200 mA g^{-1}, which is due to that the electrolyte ions cannot move to the electrode surface quickly to form an electric double layer in the limited time [39]. Moreover, the highest specific capacitance of AC-K-4 electrode reached 213 F g^{-1} with the current density of 40 mA g^{-1}. The capacitance value still keeps as high as 178 F g^{-1} at current density of 200 mA g^{-1}, which demonstrates a good rate capability. In contrast, the electrode of AC-K-4 can store a lot of energy and reveal the superior electrochemical performance.

3.2.2 CV measurement

The CV curves of AC electrodes at the scanning rates of 1 mV s^{-1} as shown in Fig. 8. Similar to the ideal CV curves of EDLC which is close to the rectangle or parallelogram shape. The CV curves of the ACs present a quasi-rectangular shape with no obvious redox peaks, demonstrating the specific capacitance derives mainly from electric double layer [40, 41]. Moreover, all the CV curves of the AC electrodes exhibit rectangular shape in the potential range of 0 to 1 V, indicating that the ACs prepared from oxygen-rich exhibit the ideal electrode materials for EDLC. In addition, the AC-K-4 has the largest area of the CV curves compare with other ACs, indicating that the AC-K-4 possess the highest specific capacitance, which is consistent with GCD result. As exhibited in Fig. 8d, with the scanning rate increasing the shape of the CV curves remained virtually unchanged, demonstrating the movement of the electrolyte ions in the pores is not limited [42, 43]. The scan rate from 1 mV s^{-1} increase to 10 mV s^{-1}, the CV curves shape of AC-K-4 is still maintain rectangle shape, which is attributed to that the highest SSA and abundance of micro- and mesopores of AC-K-4. More charge can be stored at high SSA and the micro- and mesopores is favor the transportation of the electrolyte ions.

3.2.3 EIS measurement

The Nyquist plots was used to analyze the EIS data and the results is shown in Fig. 9. A semicircle at high frequency region is related to the resistance of the charge-transfer at the electrode/electrolyte interface. The slope of line at middle frequency region should be ascribed to the diffusion of the electrolyte ions in the electrode [44]. The vertical line closed to 90° at low frequency suggesting the pure capacitive behavior and fast transfer character of electrolyte ions in the structure of the carbon electrode [45, 46]. The plots of AC electrodes display three stages: a small semicircle at high frequency, slope of line at middle frequency region and a transition to linearity at low frequency, indicating the AC electrodes have ideal electrochemical capacitance characteristic [47]. The semicircle of AC-K-4 electrode is smaller than other ACs, indicating that the ion diffusion into the electrode surface of AC-K-4 electrode is faster than others. The result reveals that the AC-K-4 electrode has a good electrochemical capacitive behavior based on the small resistance of the electrolyte.

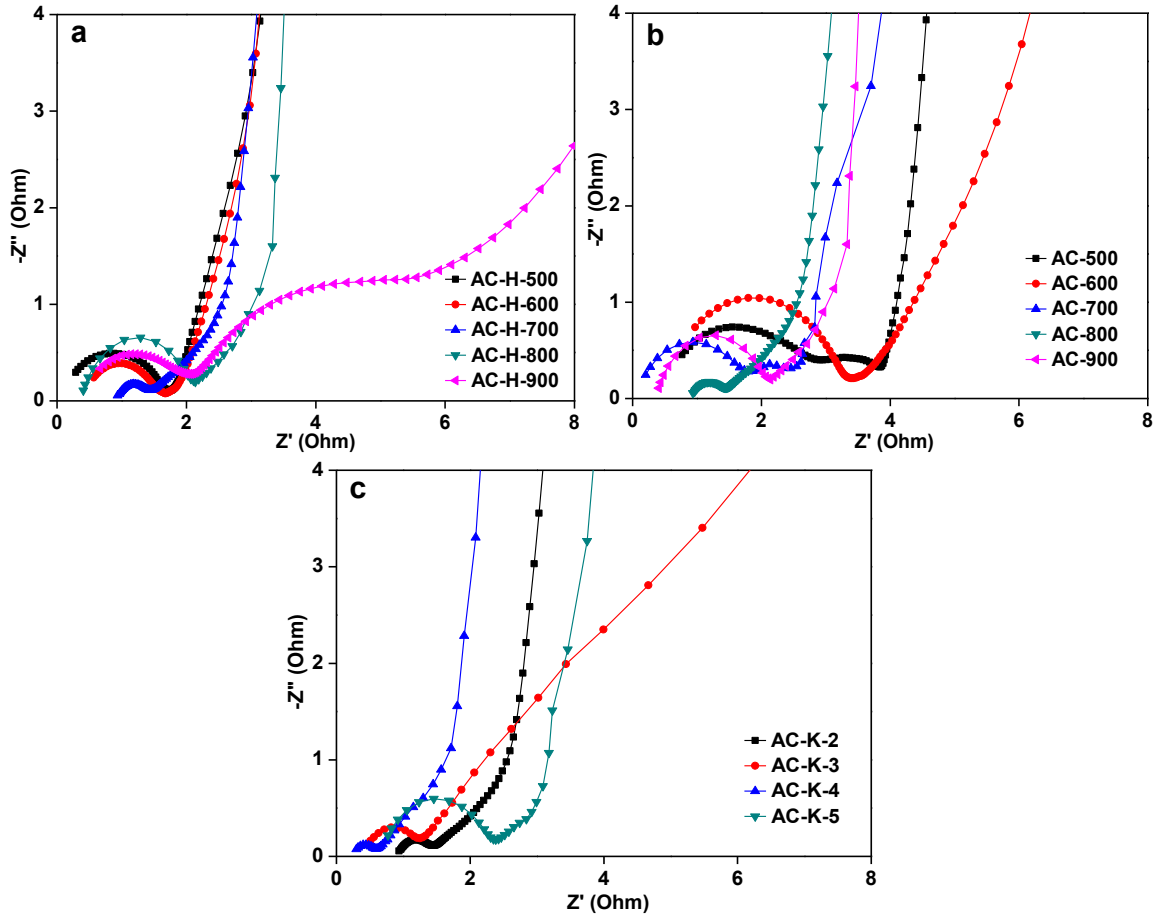

Figure 9. Nyquist plots of AC electrodes: different carbonized temperatures (a), different activated temperatures (b) and different KOH/char ratios (c).

3.2.4 Cycling life

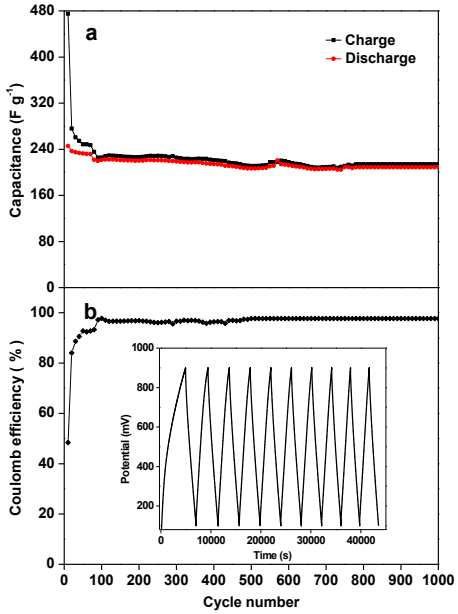

Figure 10. Cycle life of the AC-K-4 electrode at the current density of 40 mA g^{-1}: variation of the specific capacitance (a) and variation of the coulomb efficiency (b).

$$\eta = \frac{Q_{discharge}}{Q_{charge}} \times 100\% \qquad (5)$$

Where $Q_{discharge}$ is the discharge capacity, Q_{charge} is the charge capacity, respectively.

Charge-discharge is performed at the current density of 40 mA g^{-1} and the cycling life of AC-K-4 is shown in Fig. 10. After 10 cycles the specific capacitance slightly decreases from 213 F g^{-1} to 191 F g^{-1}. Because of the dissolution and detachment of the AC, the specific capacitance decreases to 176 F g^{-1} after 1000 cycles. The phenomenon demonstrates that the electrode of AC-K-4 has high capacity retention rate. The charge-discharge efficiency is evaluated according to the Eq. (5). The coulomb efficiency is 97.6% after 1000 cycles showing that the good reversibility of the AC-K-4.

4. CONCLUSION

Oxygen-rich lignite is a suitable precursor for preparing ACs with high SSA by KOH activation. The obtained ACs exhibited good electrochemical performance as EDLC electrode which due to their high SSA and appropriate pore size distribution. Carbonized temperature, activated temperature and KOH/char ratio have a great effect on the SSA and pore size distribution of ACs. The functional groups of the ACs are similar by the tested of FTIR and the OCSs of AC-K-4 are mainly C-O, C=O and -COOH through XPS analysis. The highest specific capacitance and SSA of AC-K-4 is 213 F g^{-1} at 40 mA g^{-1} and 2550 m^2 g^{-1}, respectively. In addition, the AC-K-4 also presented superior cycle stability. Further study will be focused on understanding the effect of OCSs on specific capacitance of ACs and regulation of the OCSs in ACs.

ACKNOWLEDGEMENTS
This work was subsidized by the Fundamental Research Funds for the Central Universities (China University of Mining & Technology, 2017XKZD10) and the Priority Academic Program Development of Jiangsu Higher Education Institutions.

References

1. J. R. Miller, P. Simon, *Science*, 321 (2008) 651.
2. X. Zhao, C. Johnston, P. S. Grant, *J. Mater. Chem.*, 19 (2009) 8755.
3. J. Liu, *Adv. Funct. Mater.*, 23 (2013) 924.
4. A. K. Shukla, A. Banerjee, M. K. Ravikumar, A. Jalajakshi, *Electrochim. Acta*, 84 (2012) 165.
5. A. G. Kashkooli, S. Farhad, V. Chabot, A. Yu, Z. Chen, *Appl. Energ.*, 138 (2015) 631.
6. M. B. Wu, P. Li, Y. Li, J. Liu, Y. Wang, *RSC Adv.*, 5 (2015) 16575.
7. Z. X. Tai, X. B. Yan, J. W. Lang, Q. J. Xue, *J. Power Sources*, 199 (2012) 373.
8. X. Y. Zhao, S. S. Huang, J. P. Cao, X. Y. Wei, K. Magarisawa, T. Takarada, *Fuel Process. Technol.*, 125 (2014) 251.
9. S. M. Li, S. Y. Yang, Y. S. Wang, H. P. Tsai, H. W. Tien, S. T. Hsiao, W. H. Liao, C. L. Chang, C. C. Ma, C. C. Hu, *J. Power Sources*, 278 (2015) 218.
10. C. Tran, V. Kalra, *J. Power Sources*, 235 (2013) 289.
11. S. Mezzavilla, C. Zanella, P. R. Aravind, C. Della Volpe, G. D. Sorarù, *J. Mater. Sci.*, 47 (2012) 7175.
12. X. Y. Zhao, S. S. Huang, J. P. Cao, S. C. Xi, X. Y. Wei, J. Kamamoto, T. Takarada, *J. Anal. Appl. Pyrol.*, 105 (2014) 116.

13. G. Gryglewicz, J. Machnikowski, E. Lorenc-Grabowska, G. Lota, E. Frackowiak, *Electrochim. Acta*, 50 (2005) 1197.
14. Z. Q. Hao, J. P. Cao, Y. Wu, X. Y. Zhao, Q. Q. Zhuang, X. Y. Wang, X. Y. Wei, *J. Power Sources*, 361 (2017) 249.
15. D. Hulicova-Jurcakova, M. Seredych, G. Q. Lu, T. J. Bandosz, *Adv. Funct. Mater.*, 19 (2009) 438.
16. A. Stein, Z. Wang, M. A. Fierke, *Adv. Mater.*, 21 (2009) 265.
17. J. Ren, J. P. Cao, X. Y. Zhao, F. Wei, T. L. Liu, X. Fan, Y. P. Zhao, X. Y. Wei, *Fuel*, 202 (2017) 345.
18. S. Murata, M. Hosokawa, K. Kidena, M. Nomura, *Fuel Process. Technol.*, 67 (2000) 231.
19. J. C. Wang, S. Kaskel, *J. Mater. Chem.*, 22 (2012) 23710.
20. X. Zhao, L. L. Zhang, S. Murali, M. D. Stoller, Q. H. Zhang, Y. W. Zhu, R. S. Ruoff, *Acs Nano*, 6 (2012) 5404.
21. Y. W. Zhu, S. Murali, M. D. Stoller, K. J. Ganesh, W. W. Cai, P. J. Ferreira, A. Pirkle, R. M. Wallace, K. A. Cychosz, M. Thommes, D. Su, E. A. Stach, *Science*, 332 (2011) 1537.
22. T. L. Liu, J. P. Cao, X. Y. Zhao, J. X. Wang, X. Y. Ren, X. Fan, Y. P. Zhao, X. Y. Wei, *Fuel Process. Technol.*, 160 (2017) 19.
23. G. H. An, H. J. Ahn, W. K. Hong, *J. Power Sources*, 274 (2015) 536.
24. C. Peng, X. B. Yan, R. T. Wang, J. W. Lang, Y. J. Ou, Q. J. Xue, *Electrochim. Acta*, 87 (2013) 401.
25. W. L. Zhang, M. Z. Zhao, R. Y. Liu, X. F. Wang, H. B. Lin, *Colloid. Surface. A*, 484 (2015) 518.
26. X. B. Feng, J. P. Cao, X. Y. Zhao, C. Song, T. L. Liu, J. X. Wang, X. Fan, X. Y. Wei, *J. Anal. Appl. Pyrol.*, 117 (2016) 106.
27. R. J. Mo, Y. Zhao, M. Wu, H. M. Xiao, S. Kuga, Y. Huang, J. P. Li, S. Y. Fu, *RSC Adv.*, 6 (2016) 59333.
28. Y. Wu, J. P. Cao, X. Y. Zhao, Z. Q. Hao, Q. Q. Zhuang, J. S. Zhu, X. Y. Wang, X. Y. Wei, *Electrochim. Acta*, 252 (2017) 397.
29. C. X. Zhang, D. H. Long, B. L. Xing, W. M. Qiao, R. Zhang, L. Zhan, X. Y. Liang, L. C. Ling, *Electrochem. Commun.*, 10 (2008) 1809.
30. Z. Q. Hao, J. P. Cao, X. Y. Zhao, Y. Wu, J. S. Zhu, Y. L. Dang, Q. Q. Zhuang, X. Y. Wei, *J. Colloid Interf. Sci.*, 513 (2018) 20.
31. Q. Wang, Q. Cao, X. Y. Wang, B. Jing, H. Kuang, L. Zhou, *J. Power Sources*, 225 (2013) 101.
32. B. Xu, F. Wu, Y. F. Su, G. P. Cao, S. Chen, Z. M. Zhou, Y. S. Yang, *Electrochim. Acta*, 53 (2008) 7730.
33. Y. P. Zhai, Y. Q. Dou, D. Y. Zhao, P. F. Fulvio, R. T. Mayes, S. Dai, *Adv. Mater.*, 23 (2011) 4828.
34. Z. J. Fan, J. Yan, T. Wei, L. J. Zhi, G. Q. Ning, T. Y. Li, F. Wei, *Adv. Funct. Mater.*, 21 (2011) 2366.
35. Q. G. Shao, J. Tang, Y. X. Lin, J. Li, F. X. Qin, J. S. Yuan, L. C. Qin, *J. Power Sources*, 278 (2015) 751.
36. J. Chmiola, G. Yushin, Y. Gogotsi, C. Portet, P. Simon, P. L. Taberna, *Science*, 313 (2006) 1760.
37. C. Largeot, C. Portet, J. Chmiola, P. L. Taberna, Y. Gogotsi, P. Simon, *J. Am. Chem. Soc.*, 130 (2008) 2730.
38. X. L. Gao, W. Xing, J. Zhou, G. Q. Wang, S. P. Zhuo, Z. Liu, Q. Z. Xue, Z. F. Yan, *Electrochim. Acta*, 133 (2014) 459.
39. X. J. He, N. Zhang, X. L. Shao, M. B. Wu, M. X. Yu, J. S. Qiu, *Chem. Eng. J.*, 297 (2016) 121.
40. Z. Q. Hao, J. P. Cao, Y. Wu, X. Y. Zhao, L. Zhou, X. Fan, Y. P. Zhao, X. Y. Wei, *Fuel Process. Technol.*, 162 (2017) 45.
41. Z. M. Sheng, J. N. Wang, J. C. Ye, *Micropor. Mesopor. Mater.*, 111 (2008) 307.
42. L. H. Wang, M. Toyoda, M. Inagaki, *New Carbon Mater.*, 23 (2008) 111.
43. J. C. Zhao, B. H. J. Tang, J. Cao, J. C. Feng, P. Liu, J. Zhao, J. L. Xu, *Mater. Manuf. Process.*, 27 (2011) 119.
44. Y. Wu, J. P. Cao, Z. Q. Hao, X. Y. Zhao, Q. Q. Zhuang, J. S. Zhu, X. Y. Wang, X. Y. Wei, *Int. J. Electrochem. Sci.*, 12 (2017) 7227.
45. M. Ghaemi, F. Ataherian, A. Zolfaghari, S.M. Jafari, *Electrochim. Acta*, 53 (2008) 4607.

46. Y. Wu, X. Y. Zhao, J. P. Cao, S. He, Z. Q. Hao, H. Y. Yu, G. Y. Sun, X. Y. Wei, *Int. J. Electrochem. Sci.*, 12 (2017) 8132.